

The dynamic anti-corrosion of self-derived space charge layer enabling long-term stable seawater oxidation

Jie Zhu¹, Baoguang Mao¹, Bo Wang^{*}, Minhua Cao^{*}

Key Laboratory of Cluster Science, Ministry of Education of China, Beijing Key Laboratory of Photoelectronic/Electro Photonic Conversion Materials, School of Chemistry and Chemical Engineering, Beijing Institute of Technology, Beijing 100081, PR China



ARTICLE INFO

Keywords:

Seawater electrolysis
Selenate space charge layer
Electrochemical reconstruction
Dynamic anti-corrosion
Nickel diselenide

ABSTRACT

Developing corrosion-resistant oxygen evolution electrocatalysts that can sustain seawater electrolysis is crucial but challenging for hydrogen production. Herein, we develop a bimetallic oxyhydroxide electrocatalyst with self-derived selenate space charge layer (SeO_4^{2-} SCL) by in-situ electrochemically reconstructing cobalt-doped nickel diselenide (Co-NiSe_2) pre-catalyst, enabling long-term stability for seawater electrolysis. In-situ experiments and theoretical results reveal the promoting effect of cobalt-doping on the reconstruction of NiSe_2 and generation of dynamically stable oxygen vacancy sites. Importantly, the SeO_4^{2-} SCL derived from the reconstruction process shows a dynamic anti-corrosion behavior, thus protecting metal species from dissolution and meanwhile without blocking the diffusion and adsorption of reactive species. Consequently, a two-electrode cell assembled by this Co-NiSe_2 pre-catalyst as an anode, reaches an industrial current density (500 mA cm^{-2}) at a cell voltage of 1.70 V, and that works stably for over 1500 h in alkaline seawater, which is of significance for promoting the practicality of low-cost catalysts.

1. Introduction

Electrocatalytic water splitting, involving cathodic hydrogen evolution reaction (HER) and anodic oxygen evolution reaction (OER), is considered to be the most promising method for generating clean hydrogen [1,2]. Tremendous progress has been made in employing freshwater as the electrolyte feedstock for water splitting [3,4]. However, the large-scale use of freshwater poses a serious risk of water shortage. As an inexhaustible water resource on our planet, seawater can be used to substitute freshwater, which may solve the freshwater scarcity and high-cost problems [5–8]. But numerous challenges are hindering the practical application of seawater splitting, for example, the competing of undesired pH-dependent chloride oxidation reaction (ClOR) on the anode that leads to low Faradaic efficiency of OER and the poor stability of the anode catalysts caused by chloride ion (Cl^-) corrosion [9,10]. Additionally, non-innocent ions (including anions and cations), bacteria/microbes, and small particulates present in seawater may not only decline/poison electrode/catalyst performance and long-term stability, but also dissolve the membrane used for the separation of the anode and cathode [11].

The seawater that is used to electrolyze generally is alkaline since it

needs to undergo alkali pre-treatment to remove a large amount of impurity ions (i.e. Mg^{2+} , Ca^{2+} , and so on) [11–13]. According to the Pourbaix diagram [14,15], the selectivity of OER in alkaline electrolyte systems can be improved by increasing the equilibrium potential difference between these two reactions of ClOR and OER. While OER has a lower onset potential than hypochlorite formation ($\text{Cl}^- + 2\text{OH}^- \rightarrow \text{OCl}^- + \text{H}_2\text{O} + 2\text{e}^-$, $E^0 = 1.72 \text{ V} - 0.059 \text{ pH}$ (vs. NHE)) under alkaline conditions by approximately 490 mV [16,17], practical applications require catalysts to function at industrial current densities ($\geq 500 \text{ mA cm}^{-2}$), and thus, a large overpotential may lead to increased OCl^- formation and reduced efficiency in seawater splitting. Even though the desired current density can be realized at such a low overpotential using highly active electrocatalysts, the Cl^- accumulation on the anode can severely corrode substrates and catalysts [9,18]. Therefore, rationally designing an OER catalyst with high activity, selectivity, and resistance to Cl^- corrosion is crucial yet challenging for seawater splitting.

Numerous studies have focused on creating efficient electrocatalysts for seawater splitting using transition metal-based compounds, such as oxides [19–21], hydroxides [22,23], chalcogenides [24–27], phosphides [6], and nitrides [28,29]. Similar to the process observed in freshwater electrolysis, these compounds, often acting as the pre-catalysts, also

* Corresponding authors.

E-mail addresses: bowang@bit.edu.cn (B. Wang), caomh@bit.edu.cn (M. Cao).

¹ These authors contributed equally to this work.

undergo surface reconstruction in alkaline seawater splitting, thus leading to the formation of metal oxyhydroxides that have been identified as the actual active species for OER [30–32]. Generally, reducing the activation energy barrier for initiating surface reconstruction and improving the intrinsic activity of formed metal oxyhydroxides are critical for achieving high electrocatalytic performance of the reconstructed catalysts [33–35]. For instance, further doping the metal oxyhydroxides with heteroatoms can manipulate the adsorption energy of oxygen-containing intermediates on the active sites to promote the OER activity [34,36]. Unfortunately, the highly active metal oxyhydroxides can be easily corroded by Cl^-/ClO^- during the high-current-density operation, thus greatly impacting their activity and lifespan in seawater splitting [37,38]. In this connection, it was found that introducing a protective layer on the electrode surface is an effective strategy to avoid severe Cl^-/ClO^- corrosion. For example, the direct addition of negatively charged anions into electrolytes can form a protective layer at the surface of the Fe/Co/Ni-based electrodes to repel Cl^-/ClO^- in seawater [18,39,40], thus improving their corrosion resistance. However, the inevitable competitive adsorption between the added anions and chloride ions from the beginning is energetically unfavorable; moreover, the surface/interfacial chemical behaviors of these anions adsorbed on the surface have always been confusing [26,33]. Although these findings point to the critical role of anions as corrosion inhibitors, the dynamic anti-corrosion behavior of anions in seawater, especially those in situ self-derived at the electrode/electrolyte interface, has been rarely investigated.

Herein, by utilizing in-situ electrochemical reconstruction of a doping-engineered pyrite-type diselenide pre-catalyst, we develop a highly efficient and stable bimetallic oxyhydroxide seawater electrocatalyst, in which the self-derived selenate space charge layer (SeO_4^{2-} SCL) on its surface is able to prevent Cl^- from approaching the dynamically generated active sites. In-situ experiments and theoretical investigations verify that the cobalt doping for nickel diselenide (Co-NiSe_2) facilitates its rapid reconstruction process to form highly active cobalt-doped nickel oxyhydroxide (Co-NiOOH) by reducing the energy barriers of de-selenium and de-hydrogenation and meanwhile contributes to the generation of dynamically stable oxygen vacancy sites in resultant Co-NiOOH , enabling high OER performance. Furthermore, the self-derived SeO_4^{2-} SCL at the electrode surface displays a dynamic anti-corrosion behavior, i.e. selectively repelling Cl^- ions without blocking the diffusion and adsorption of reactive species and thus preventing metal species in Co-NiOOH from being dissolved. As a result, this restructured Co-NiSe_2 can deliver an industrial current density (500 mA cm^{-2}) at a cell voltage of 1.70 V with ~100% O_2 Faradaic efficiency in a two-electrode electrolyzer, and that operates stably for over 1500 h in real seawater electrolyte. This work provides a novel perspective toward understanding the protection mechanism of anions for OER electrocatalysts and would enlighten the development of simple yet efficient strategies to address the challenges in seawater electrolysis.

2. Experimental section

2.1. Materials preparation

Synthesis of Co-NiSe_2 nanospheres: In a typical synthesis, $\text{Ni}(\text{NO}_3)_2 \cdot 6 \text{ H}_2\text{O}$ and $\text{Co}(\text{NO}_3)_2 \cdot 6 \text{ H}_2\text{O}$ (with a molar ratio of Co to Ni of 1:3) were dissolved in a mixed solution of glycerol (8 mL) and isopropanol (40 mL) under constant stirring. Subsequently, the obtained mixed solution was transferred into an 80 mL Teflon-lined stainless steel autoclave and kept at 180 °C for 12 h. After being cooled to room temperature, the Co-Ni-alkoxide precursor product was separated by centrifugation and washed with ethanol several times. Then, the Co-Ni-alkoxide precursor was further selenized (the mass ratio of precursor to selenium powder is 1:10) in a tube furnace under an ultra-purity N_2 atmosphere at 400 °C for 2 h to obtain the final Co-NiSe_2 nanospheres.

Synthesis of CoSe_2 and NiSe_2 nanospheres: For comparison, single-

component CoSe_2 and NiSe_2 spheres were also prepared with reaction parameters similar to those of the Co-NiSe_2 nanospheres. The difference is that the precursor synthesis process uses only one component salt.

Synthesis of Co-NiO nanospheres: The Co-Ni-alkoxide precursor synthesized by the solvothermal method was directly calcined at 400° for 2 h under air to obtain the Co-NiO nanospheres.

2.2. Materials characterizations

The phase structure was detected by X-ray diffraction (XRD, Bruker D8) equipped with Cu K_α radiation ($\lambda = 1.54056 \text{ \AA}$) at 40 kV and 40 mA at a scanning rate of 5°/min. The morphologies and microstructures of the samples were characterized by field emission scanning electron microscopy (FE-SEM, HITACHI S-4800) at 2 kV and transmission electron microscope (TEM, JEOL JEM-2010) working at 100 kV, respectively. High-resolution TEM (HR-TEM) and high-angle annular dark-field scanning TEM (HAADF-STEM) were carried out by a JEOL JEM-2100F field emission electron microscope. Energy dispersive X-ray (EDX) mapping images were taken under HAADF-STEM mode, which was operated at 200 kV. Raman spectra were collected on an Invia Raman spectrometer with an excitation laser wavelength of 532 nm. The element contents of the samples were determined by inductively coupled plasma-optical emission spectroscopy (ICP-OES) (PerkinElmer). X-ray absorption spectroscopy (XAS) measurements were undertaken at Beamlines 1W1B at Beijing Synchrotron Radiation Facility (BSRF). X-ray spectroscopy (XPS) was performed on ESCALAB 250 spectrometer (Perkin-Elmer).

2.3. Electrochemical measurements

Preparation of electrocatalyst ink: The working electrode for electrochemical measurements was prepared by dispersing 5 mg of catalyst powder into 1 mL of solution containing 900 μL of ethanol and 100 μL of Nafion solution (5 wt%), followed by ultrasonication for 30 min to obtain a homogeneous slurry. Then, 20 μL of slurry was coated onto a glassy carbon (GC) electrode ($D = 5 \text{ mm}$) and dried naturally under room temperature.

OER measurements: The OER performances were evaluated in a standard three-electrode configuration using a CHI 760E electrochemical workstation (CH instrument, Chenhua). Wherein a graphite rod electrode and Hg/HgO electrode were used as the counter electrode and the reference electrode, respectively. Linear sweep voltammetry (LSV) curves of OER measurements were taken at a scan rate of 5 mV s^{-1} in 1 M KOH + 0.5 M NaCl solution. The cyclic voltammetry (CV) was obtained under potentials from 0.924 to 1.624 V (vs. RHE) at a scan rate of 50 mV s^{-1} . The potentials measured were referenced to a reversible hydrogen electrode (RHE) according to the Nernst equation: $E(\text{RHE}) = E(\text{Hg}/\text{HgO}) + (0.098 + 0.059 \text{ pH}) \text{ V}$. According to the Tafel equation, the Tafel slope was obtained from the corresponding LSV curves. *Operando* EIS plots were collected from 1.2 to 1.5 V in a frequency range of 0.01 Hz to 1 MHz and amplitude of 10 mV. The long-term durability was conducted by chronoamperometric curves with a current density of 500 mA cm^{-2} in 1 M KOH + 0.5 M NaCl solution or 1 M KOH seawater in a constant-temperature test chamber. To avoid voltage fluctuation to the greatest extent, we slowly injected the electrolyte into the inner wall of the electrolyzer with a miniature syringe every day to keep the electrolyte volume constant. The seawater was taken from Bohai (China) and purified with 1 M KOH to remove Ca^{2+} , Mg^{2+} and so on before testing.

Double layer capacitances (C_{dl}) were estimated by measuring the CV under different scan rates (20–100 mV s^{-1}) in a non-faradaic region. Electrochemical active surface area (ECSA) was calculated by equation: $\text{ECSA} = C_{dl} / C_s$, where C_s is the specific capacitance of a sample under the specific condition of electrolyte. Here, we chose an average value (0.04 mF) to get the average value of ECSA of our catalyst. The surface concentration of metal atoms was determined from the CV curve.

Determination of turnover frequency (TOF) was from the integrated OER polarization curve. The equation of TOF is $\text{TOF} = (i \times N_A) / (A \times F \times n \times r)$, where i , N_A , A , F , n , and r are rare current, Avogadro number, geometrical surface area of electrode, Faraday constant, number of electrons, and surface concentration of atoms, respectively. The water displacement method was used for the quantification of molecular O_2 and H_2 . The measured volume was then converted into faradic efficiency (FE) by comparing with theoretical yield using the formula — $\text{FE} = V_{\text{experimental}} / V_{\text{theoretical}}$. While $V_{\text{theoretical}} O_2 = Q \times V_m / n \times F$, where V_m is the molar volume of gas and Q is the amount of electric charge.

2.4. In-situ measurements

In-situ XAS was performed at the 1W1B beamline of the BSRF, China. The storage ring of BSRF was operated at 2.5 GeV with a maximum electron current of 250 mA. In-situ XAS measurements were performed with catalyst-coated carbon cloth using a home-built cell. The catalyst powder was dispersed in ethanol with 20 μL of Nafion solution (5%, Sigma-Aldrich), and then sonicated for 30 min. The catalyst ink was dropped onto carbon paper taped with Kapton film on the back as the working electrode ($\sim 1 \text{ cm} \times 1 \text{ cm}$) to ensure the electrocatalyst was in full contact with the KOH electrolyte at a geometric catalyst loading of $\sim 0.5 \text{ mg cm}^{-2}$. The electrode is positioned in front of the Kapton window to give the minimum possible path length through the electrolyte. The cell was purged with Ar for 15 min before starting experiments. The XAS spectra were collected through fluorescence mode. During XAS measurements, we calibrated the position of the absorption edge (E_0) using Co/Ni foil, and all the XAS data were collected during one period

of beam time. The position of E_0 is defined as the point corresponding to the maximum value in the derivative curves of the X-ray absorption near edge structure (XANES) spectra. The raw data analysis was performed using the IFEFFIT software package according to the standard data analysis procedures.

In-situ Raman spectroscopy measurements: Raman spectra of samples were recorded using the confocal Raman spectrometer (LabRAM Aramis) equipped with a 532 nm laser. A custom-made electrochemical cell (Gaossunion (China, Tianjin) Photoelectric Technology Co., Ltd.) was used for in-situ experiments, where a fluorine-doped SnO_2 substrate coated with the catalyst was used as the working electrode, platinum wire, and Ag/AgCl electrode as the counter and reference electrodes, respectively. An electrochemical workstation (CHI 760E, Chenhua) was used to apply potentials to the working electrode while Raman spectra were acquired.

In-situ FT-IR (Nicolet iS20 FT-IR Spectrometer, Thermo Fisher Scientific) spectra were collected during the oxygen evolution reaction (OER) process (from initial to 1.55 V at a scan rate of 3 mV s^{-1} in the electrolyte), where a copper current collector coated with the catalyst was used as the working electrode, a platinum wire, and a Hg/HgO electrode as the counter and reference electrodes, respectively.

3. Results and discussion

3.1. Theoretical understanding of the underlying driving force of reconstruction

The pre-catalyst design starts with a pyrite-type transition-metal

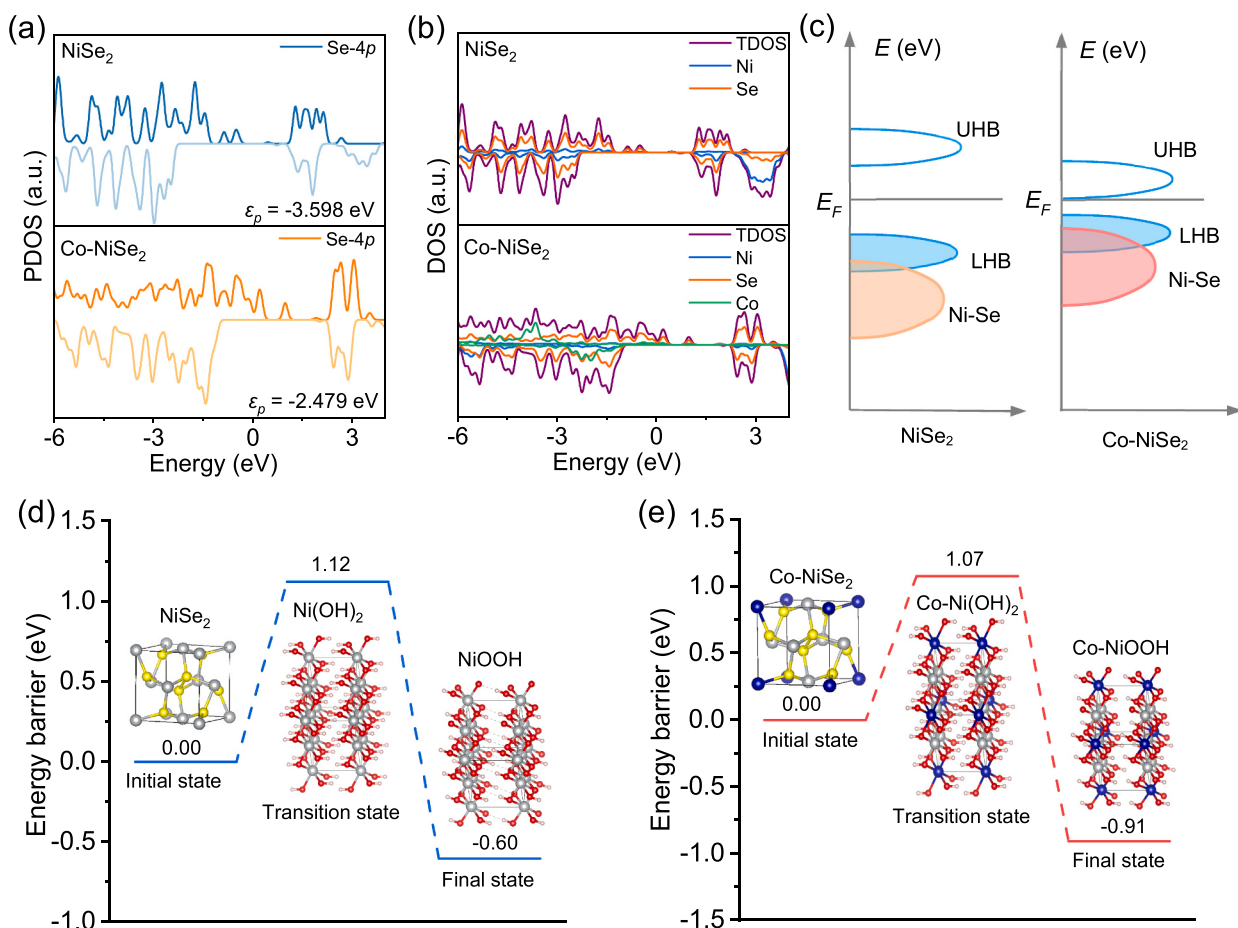
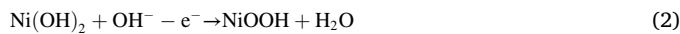
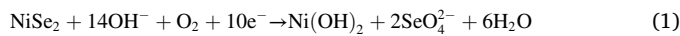


Fig. 1. (a) Computed projected density of state (PDOS) of Se 4p and (b) total density of state (TDOS) for NiSe₂ and Co-NiSe₂. (c) Schematic illustration of band diagrams for NiSe₂ and Co-NiSe₂. DFT-calculated reaction energy barriers of de-selenization and de-hydrogenation processes for (d) NiSe₂ and (e) Co-NiSe₂. The H, O, Se, Ni, and Co atoms are represented by pink, red, yellow, grey, and blue balls, respectively.

dichalcogenide (TMD). It has been well addressed that the reconstruction of TMDs under alkaline OER conditions is limited due to their poor structural flexibility [33,41,42]. As a member of TMDs, NiSe₂ was selected and its electronic structure first was investigated by density functional theory (DFT) calculations. The computational models for NiSe₂ are presented in Fig. S1 (for modeling see Supporting Information). As revealed by the band center energy (Fig. 1a, upper), the physical origin of the limited reconstruction of NiSe₂ is due to its low Se 4p-band center energy level relative to the Fermi level, consistent with the results reported in the literature [33]. It was proposed previously that raising the O 2p-band center level of oxides can activate the reactivity of lattice oxygen for OER, thereby improving structural flexibility for reconstruction [43]. Given this, it is highly desirable for TMDs to uplift the anionic p-band center level to obtain more structural flexibility for reconstruction. Here, Co-doping engineering is employed to elevate the Se 4p-band central energy level to promote the reconstruction of NiSe₂. As shown in Fig. 1b, the electronic state of NiSe₂ after Co-doping (Co-NiSe₂) around the Fermi level is evidently higher than that of NiSe₂, implying greater orbital hybridization of the elements, thereby accelerating the charge transfer in the electrochemical OER reaction. Moreover, the Se 4p band of Co-NiSe₂ is elevated to a higher energy level and its center is closer to the Fermi level than that of the Se 4p in NiSe₂ (Fig. 1a, lower), indicating that the Se atoms in Co-NiSe₂ have high reactivity and are more susceptible to oxidative leaching along the anodic potential sweep. For later transition metals, M-Se orbitals tend to be split by strong d-d orbital interactions, resulting in one empty upper-Hubbard band (UHB) and one filled lower Hubbard band (LHB) [44]. In an anodic sweep, the electrons will be removed from the LHB first, resulting in an increased oxidation state of metal cations. Since the Se 4p in Co-NiSe₂ is at a high energy level relative to that in NiSe₂, the Ni-Se orbitals are close to the Fermi level (Fig. 1c). This will lead to the fast removal of electrons from Ni-Se bonding orbitals following the oxidation of metal cations for Co-NiSe₂, thus causing the breaking of Ni-Se bonds and facilitating the formation of oxyhydroxide and the oxidative leaching of Se species during the OER [33].

To induce a phase reconstruction of NiSe₂ into oxyhydroxide, the de-selenium and de-hydrogenation behaviors in the structural domain are considered to be two critical conditions. Therefore, the de-selenium and de-hydrogenation kinetics of the two pre-catalysts were investigated by estimating their activation energy barriers. Based on the electrochemical processes of the OER, we conceive the plausible reaction paths as follows:



Specifically, the hydroxide and selenate are first formed via a full de-selenium process (Equation 1), and then the oxyhydroxide species is further generated through the de-hydrogenation process (Equation 2). DFT energetics for these two paths were obtained under the polarization potential of 1.6 V vs. RHE, as shown in Fig. 1d,e. It can be seen that the de-selenium process of Co-NiSe₂ gets thermodynamically favorable relative to that of the pristine NiSe₂, and more importantly, the de-hydrogenation energy barrier decreases significantly from -0.60 eV for NiSe₂ to -0.91 eV for Co-NiSe₂, suggesting a faster reconstruction reaction kinetics for Co-NiSe₂. From the above results, it can be concluded that the introduction of Co effectively optimizes the local electronic configurations of the NiSe₂ pre-catalyst and meanwhile reduces its activation energy barrier for reconstruction. This will energetically promote the phase reconstruction process, as discussed below.

3.2. Structure and composition characterizations

Based on the above theoretical prediction, NiSe₂ and Co-NiSe₂ were synthesized via a solvothermal method followed by selenization

treatment to experimentally validate the Co-doping effect on phase reconstruction (Figs. S2-S4). Fig. 2a presents the XRD pattern of the as-prepared sample, which shows a standard pyrite-type cubic NiSe₂ structure (JCPDS No. 41-1495). Besides, it was found that the strongest diffraction peak of Co-NiSe₂ exhibits an obvious shift toward a higher angle relative to that of the pristine NiSe₂ (the inset in Fig. 2a), which is the result of partial nickel being replaced by cobalt. This structural change caused by Co doping was further reflected by the Raman spectra, in which Co-NiSe₂ shows similar Raman vibrations but with a slight red shift relative to those of NiSe₂ (Fig. 2b). TEM images of Co-NiSe₂ reveal its spherical structure (Fig. S5 and Fig. 2c). HR-TEM image shows clear lattice fringes with lattice spacings of 0.27 nm, corresponding to the (210) plane of the NiSe₂ phase (Fig. 2d), and the Co, Ni, and Se elements distribute uniformly on the entire nanosphere (Fig. 2e). To disclose how the Co incorporation tailors the local coordination environment and electronic configurations of NiSe₂, XANES and extended X-ray absorption fine-structure (EXAFS) measurements at both Ni and Co K-edges were performed. The Ni K-edge spectra (Fig. 2f, left) show that the Ni states in the as-prepared NiSe₂ and Co-NiSe₂ are close to that of the NiO reference, suggesting that the valence state of Ni is approximately divalent. However, the Ni K-edge of Co-NiSe₂ exhibits a negative shift compared with that of NiSe₂, indicating that the valence state of Ni decreases after the Co doping. In the Ni K-edge EXAFS spectra (Fig. 2f, right), the characteristic peak at ~2.14 Å is ascribed to the Ni–Se bond, and it is weakened after the Co doping, implying the formation of Se vacancies (Se_v). Compared to NiSe₂ with a featureless EPR signal, Co-NiSe₂ shows a strong EPR signal, further confirming rich Se_v involved in Co-NiSe₂ (Fig. 2g). Moreover, DFT calculations reveal that the Co doping for NiSe₂ is more conducive to the formation of Se_v since Co-NiSe₂ has lower formation enthalpy of vacancies (Fig. 2h). The lower oxidation state of Ni with the Se_v will be beneficial to promote the phase reconstruction of Co-NiSe₂ [34]. Unlike the case of Ni, the Co K-edge XANES spectra show that the Co valence state in Co-NiSe₂ is lower than that in the pristine CoSe₂ along with a dominant Co²⁺ (Fig. S6), and the intensity of the Co–Se bond (~2.1 Å) from the corresponding EXAFS spectrum is also distinguished from that in the pristine CoSe₂, which can be attributed to the effect of Se_v formation. Combining all the XAS data, it can be concluded that the Co doping for NiSe₂ effectively modulates the local electronic configurations, which is expected to promote the reconstruction and increase the content of active oxyhydroxide species, thereby providing more abundant active sites for the OER.

3.3. In-situ spectroscopies for monitoring the reconstruction process

To activate the OER activity of the as-prepared pre-catalyst, the CV tests were performed in a standard three-electrode system in 1 M KOH. Earlier studies have revealed the importance of the pre-oxidation of Ni²⁺ in oxides for the OER, and Ni²⁺ is inclined to be oxidized to Ni³⁺ or a high oxidation state, which is believed to be a critical step to generate active Ni oxyhydroxide species for OER [43]. The first and second CV cycles were used to study the pre-oxidation of Ni²⁺ in Co-NiSe₂ and NiSe₂ (Fig. S7). For both Co-NiSe₂ and NiSe₂, the first cycle displays a larger pseudocapacitive charge than the second cycle, demonstrating that these two catalysts undergo an irreversible surface reconstruction into oxyhydroxide. Notably, the oxyhydroxide formation here displays different pseudocapacitive behaviors depending on the presence of Co or not. To be specific, the anodic peak of Ni²⁺ to Ni³⁺ attributed to the oxidation of the Ni–Se bond in the first cycle appears at ~1.39 V for Co-NiSe₂, while this anodic peak is more positive for NiSe₂ (~1.43 V), suggesting that Co-doping has a promoting effect on the pre-oxidation of Ni in Ni–Se bond and facilitates the subsequent formation of Ni oxyhydroxide. As observed in the OER region, the overpotential for triggering the OER by Co-NiSe₂ is greatly reduced at the second cycle while almost no such difference is detected between the first and second cycles for NiSe₂, indicating that the reconstruction process in the presence of Co-doping is a critical step for OER. In the subsequent cycles, the

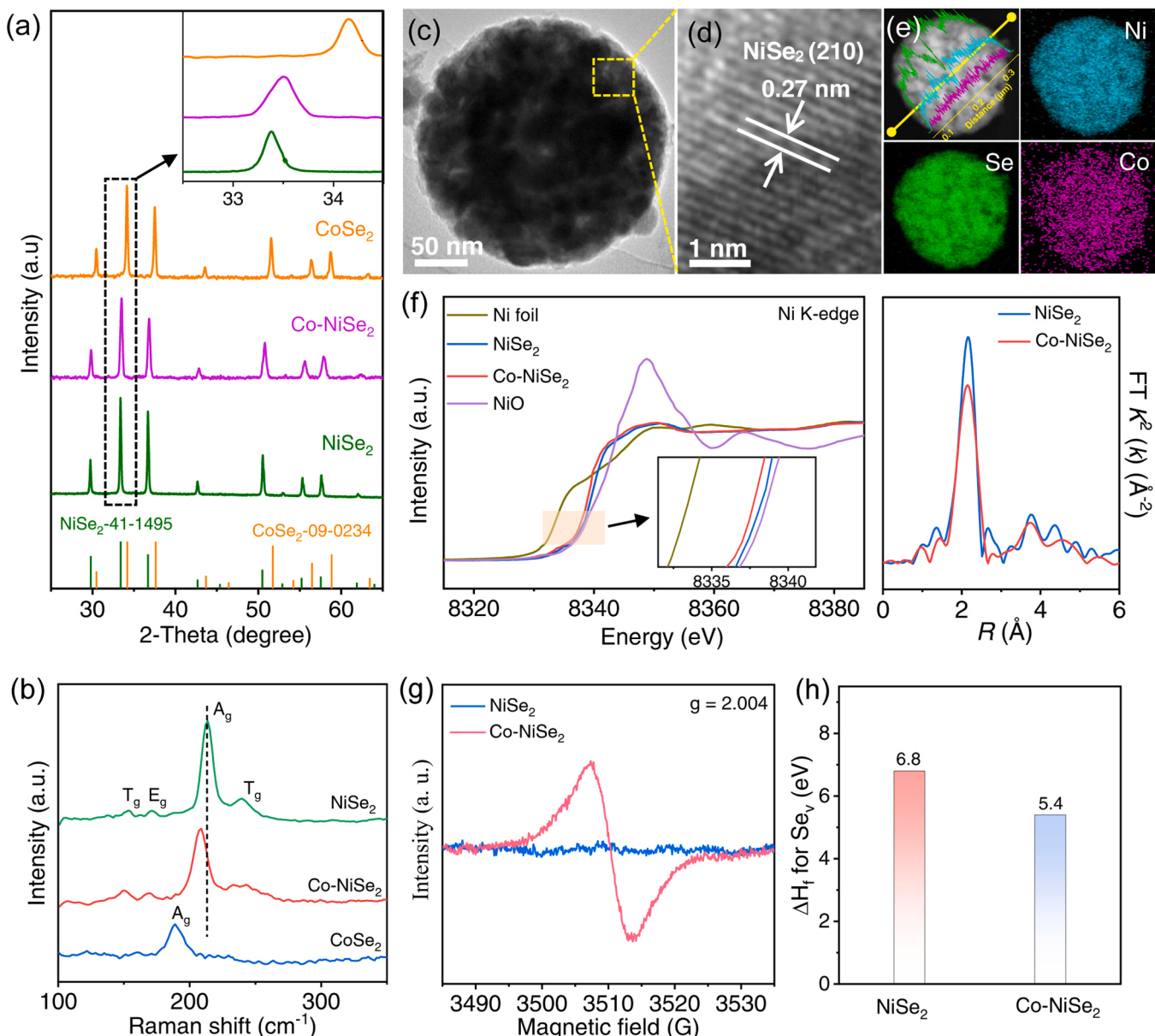


Fig. 2. (a) Powder XRD patterns and (b) Raman spectra of the synthesized Co-NiSe₂, NiSe₂, and CoSe₂ samples. Inset: the magnified XRD patterns in the range between 32.5° and 34.5°. (c) TEM and (d) HR-TEM image of Co-NiSe₂. (e) HAADF-STEM image and corresponding EDX mappings as well as line-scanning images of Co-NiSe₂. (f) The Ni K-edge XANES (left) and EXAFS (right) spectra of Co-NiSe₂, NiSe₂, and reference samples. (g) EPR spectra of Co-NiSe₂ and NiSe₂. (h) The formation enthalpy ΔH_f for the Se_v of Co-NiSe₂ and NiSe₂.

Co-NiSe₂ and NiSe₂ pre-catalysts exhibit a different dynamic self-optimization process (Fig. S8). For Co-NiSe₂, the OER current density increases sharply at the beginning, then gradually slows down, and finally stabilizes after ≈ 90 cycles (Fig. 3a). In contrast, NiSe₂ presents a slow change in the OER activity during cycling. Obviously, the dynamic self-optimization trend of Co-NiSe₂ is greater than that of NiSe₂, again confirming that incorporating Co into the Co-NiSe₂ pre-catalyst promotes the self-restructuring process during the electrochemical activation. Thus, a faster reconstruction will happen on the Co-NiSe₂.

To explore the reconstruction process of Co-NiSe₂, in-situ XAS spectra at the Ni and Co K-edge were collected during the OER process at various electrochemical potentials. From the XANES spectra (Fig. 3b), it can be found that the position of the absorption edge for the Ni K-edge in Co-NiSe₂ positively shifts with the applied potential increasing from 1.10 to 1.55 V, suggesting that the Ni species is oxidized to higher oxidation states accompanied with a dynamic reconstruction process

during the OER. Notably, the Ni K-edge moves significantly at 1.25 V relative to 1.10 V, and its position is close to that of the standard Ni(OH)₂ reference, manifesting that the Co-NiSe₂ pre-catalyst undergoes an obvious structural change and in-situ evolves into Ni(OH)₂. In the subsequent applied potentials, the position of the Ni K-edge shifts toward high energies close to that of the standard γ -NiOOH reference, indicating that the generated Ni(OH)₂ is further evolved into γ -NiOOH. The coordination environment of the Ni site in Co-NiSe₂ was further investigated by the Ni K-edge EXAFS spectra during the OER process (Fig. 3c). It is obvious that the initial Ni–Se bond strength in Co-NiSe₂ drops at 1.10 V and then further disappears at 1.25 V, while a new peak, attributed to the Ni^{II}–O bond of the in-situ generated Ni(OH)₂, appears at 1.48 Å at 1.10 V and further enhances at 1.25 V. Meanwhile, another important feature appearing at 2.46 Å is assigned to the radial distance of Ni^{II}OH (Ni^{II} in octahedron) to its neighboring metal atom (abbreviated as Ni^{II}–M, M stands for Ni or Co) in the hydroxide. The formation of the

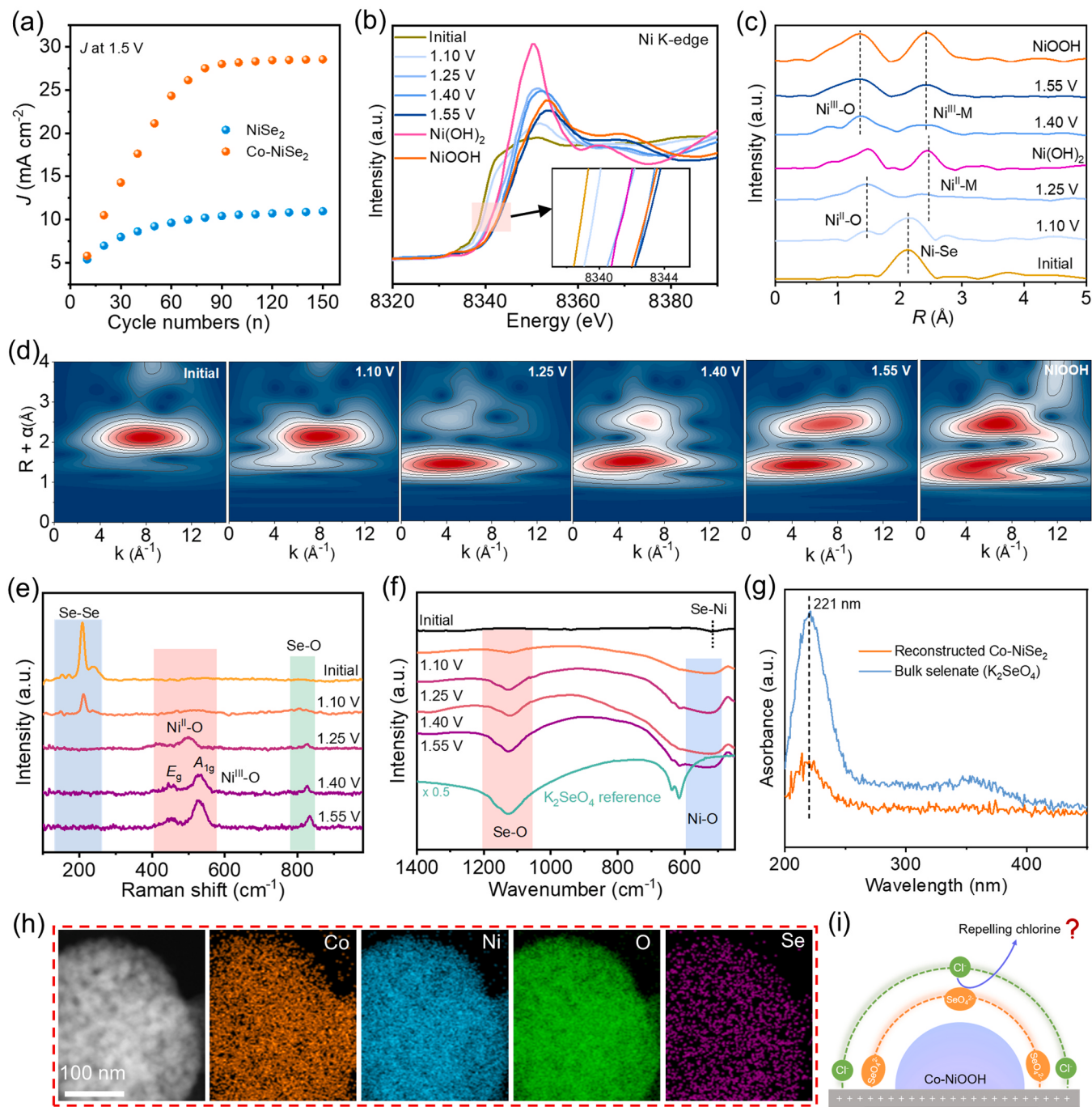


Fig. 3. (a) Comparison of the current densities with the increase of CV cycle at a potential of 1.5 V vs. RHE. In-situ Ni K-edge XANES (b) and Ni K-edge EXAFS (c) spectra of Co-NiSe₂ under initial, 1.10, 1.25, 1.40, and 1.55 V with standard Ni(OH)₂ and NiOOH as the references. The inset in (b) shows a detailed view of the rectangular shaded section. (d) The corresponding WT contour plots. (e) In-situ Raman and (f) FT-IR spectra of Co-NiSe₂ under initial, 1.10, 1.25, 1.40, and 1.55 V. (g) UV-vis spectra of the reconstructed Co-NiSe₂ electrode and bulk selenate (K_2SeO_4). (h) HAADF-STEM image and corresponding EDX mappings of the reconstructed Co-NiSe₂ electrode. (i) The schematic illustration of the reconstruction of Co-NiSe₂ to generate Co-NiOOH and SeO_4^{2-} SCL on the surface.

$Ni^{II}-O$ and $Ni^{II}-M$ bonds reveals the transformation of diselenide to hydroxide during the OER process. As the potential is further increased to 1.40 V, the $Ni^{III}-O$ bond is observed and shortened relative to the $Ni^{II}-O$ bond, which is the result of the conversion of the hydroxide to the corresponding oxyhydroxide [18]. Relative to the case at 1.40 V, the intensities of the $Ni^{III}-O$ and $Ni^{II}-M$ peaks in the formed oxyhydroxide become stronger at 1.55 V, but are lower than those of the standard NiOOH, implying the lower coordination number and the formation of the oxygen vacancies (O_v) in the oxyhydroxide during the reconstruction. This was further confirmed by the EPR (Fig. S9a) and

high-resolution O 1 s XPS spectroscopies (Fig. S9b), and in the EPR spectroscopy an obvious signal at $g = 2.003$ is observed for the reconstructed Co-NiSe₂, suggesting the in-situ generated O_v , which can greatly improve OER performance [38]. These dynamic chemical bonding changes during the reconstruction process were visualized by the wavelet transform (WT) of the EXAFS spectra (Fig. 3d and Fig. S10). The WT results witness the in-situ evolution of Co-NiSe₂ to γ -NiOOH through the disappearance of the initial Ni–Se bond and the formation of the final $Ni^{III}-O$ and $Ni^{III}-M$ bonds, in good agreement with the results of EXAFS, which also were confirmed by in-situ XPS of Ni

(Fig. S11a). In contrast, the Ni K-edge EXAFS spectrum of NiSe₂ still shows a stronger Ni–Se bond upon applying a potential to 1.25 V (Fig. S12), although its Ni K-edge XANES spectrum also shifts to a high-energy position. This result strongly demonstrates that the self-construction of NiSe₂ is dynamically sluggish without the facilitating effect of Co-doping. In addition, the local structural evolution of Co was also monitored by the Co K-edge XAS spectra (Fig. S13). With increasing the potential from 1.10 to 1.55 V, the position of the absorption edge for the Co K-edge positively moves, indicating that the Co species is also oxidized to higher oxidation states. Moreover, the Co K-edge EXAFS spectra and their WT results also reveal the dynamic evolution of the initial Co–Se bond to the final Co^{III}–O and Co^{III}–M bonds, consistent with in-situ XPS results of Co (Fig. S11b). This same local structural evolution trend between the Ni and Co atoms ultimately contributes to the formation of highly active Co-NiOOH with O_v.

To further identify the active phase and dynamic reconstruction of Co-NiSe₂, in-situ Raman and FT-IR spectroscopies were performed as the function of applied potential. For the in-situ Raman spectra, the characteristic Raman peaks of Co-NiSe₂ completely vanish at 1.25 V (Fig. 3e), while for NiSe₂, the typical A_g peak still appears at this potential (Fig. S14), which was also corroborated by in-situ XAS spectra. Meanwhile, for Co-NiSe₂, a well-defined Raman band at 498.9 cm⁻¹ is detected and it is attributable to the Ni^{II}–O vibration of Ni(OH)₂ [18]. At more positive potentials, this band feature splits into a pair of peaks at 451.6 and 526.4 cm⁻¹, which are attributed to E_g bending and A_{1g} stretching vibration of Ni^{III}–O in NiOOH, respectively [18]. TEM images of Co-NiSe₂ after reconstruction also confirm the formation of a low-crystalline γ-NiOOH phase with short-range ordered lattice fringes (Fig. S15). Besides, at 1.25 V, a new Se–O band belonging to selenate (SeO₄²⁻) is observed at 828.2 cm⁻¹ [45], which is the result of the in-situ formation of SeO₄²⁻ by the de-selenium process of NiSe₂ on the electrode surface. And this Se–O band enhances slowly with increasing the potential, indicating that more SeO₄²⁻ anions enrich on the electrode surface because of the charged nature of the anode and the electric field. This change trend for the Se–O band is also found in in-situ FT-IR spectra of Co-NiSe₂ (Fig. 3f), where an absorption band of the symmetric stretching of SeO₄²⁻ at ~1128 cm⁻¹ is observed. Therefore, the in-situ Raman and FT-IR spectra both demonstrate that the Co-NiSe₂ can evolve rapidly into the active Co-NiOOH phase during the reconstruction, simultaneously accompanied with the formation of SeO₄²⁻ species on the electrode surface. The in-situ formation of SeO₄²⁻ on electrode surface is also further confirmed by Se 3d XPS spectrum (Fig. S16) and solid ultraviolet-visible (UV-vis) absorption spectroscopy (Fig. 3g) of the reconstructed Co-NiSe₂ electrode [46,47]. Moreover, we also detected free SeO₄²⁻ anions in electrolyte by the liquid UV-vis absorption spectroscopy (Fig. S17), indicating that the in-situ formed SeO₄²⁻ on electrode surface partially diffused into the electrolyte. Notably, HAADF-STEM image and corresponding EDX mappings (Fig. 3h) on reconstructed Co-NiSe₂ electrode further disclose the presence of SeO₄²⁻ species. It is worth noting that the selenium signal on reconstructed Co-NiSe₂ electrode comes from in-situ formed SeO₄²⁻ species rather than selenium species of the unreconstructed or residual Co-NiSe₂ electrode because the Co-NiSe₂ electrode has been completely converted into Co-NiOOH based on the previous in-situ spectral results (Fig. 3c-f). Thus, combining these results with in-situ Raman and FT-IR, it can be deduced that the SeO₄²⁻ ions formed at the lower potential are present on the electrode surface and gradually increase with increasing the potential, thereby establishing a SeO₄²⁻ SCL on the electrode surface (Fig. 3i), which is expected to be able to repel chloride in seawater electrolysis.

3.4. The OER performance of the reconstructed catalysts in alkaline seawater

The above results demonstrate theoretically and experimentally that the Co-doping for NiSe₂ facilitates its reconstruction to produce the Co-NiOOH phase, which is one of the widely recognized active species for

OER [33], and the self-derive SeO₄²⁻ SCL on the electrode surface is expected to repel chloride ions during seawater electrolysis. In view of this, we cannot wait to examine the OER activity of the anodically activated Co-NiSe₂ (denoted as A-Co-NiSe₂) with self-derived SeO₄²⁻ SCL in alkaline simulated seawater electrolyte (1 M KOH + 0.5 M NaCl). Similar to the activation of Co-NiSe₂, the activated NiSe₂ (A-NiSe₂) and Co-NiO (A-Co-NiO), as well as the benchmark IrO₂ were used as controls for comparison. It is noted that the Co-NiO catalyst evolves into an active Co-NiOOH phase after CV activation under alkaline conditions as well (Figs. S18,S19). And after the above catalysts were activated, 0.5 M NaCl was added to 1 M KOH solution to further test their OER catalytic performance in alkaline simulated seawater. As shown in Fig. 4a, A-Co-NiSe₂ displays excellent activity towards OER with a small overpotential of 225 mV at 10 mA cm⁻² (η_{10}), which is significantly lower than those of A-NiSe₂ (290 mV), A-Co-NiO (260 mV), and IrO₂ (270 mV). The mass activities of catalysts were normalized by the total mass of the loaded metal (Ni or/and Co). As can be observed from Fig. S20, A-Co-NiSe₂ reaches 194.0 A g_{Co+Ni}⁻¹ at 1.5 V, which is evidently higher than those of A-NiSe₂ (68.8 A g_{Ni}⁻¹) and A-Co-NiO (128.1 A g_{Co+Ni}⁻¹), suggesting its excellent OER intrinsic activity. To further reveal the intrinsic catalytic behavior, the TOF for the O₂ molecule evolution over A-Co-NiSe₂ was calculated to be 22.8 s⁻¹ at 1.5 V (Fig. S21) and this value is greater than those of A-NiSe₂ (7.2 s⁻¹) and A-Co-NiO (15.2 s⁻¹). This outstanding intrinsic activity of A-Co-NiSe₂ is attributed to the reconstruction-generated Co-NiOOH with abundant O_v. In addition, the OER activities of A-Co-NiSe₂ and A-NiSe₂ in 1 M KOH + 0.5 M NaCl are almost the same as those in 1 M KOH, while the OER activity of A-Co-NiO in 1 M KOH + 0.5 M NaCl is inferior to that in 10 M KOH (Fig. S22). Specifically, at 50 mA cm⁻², the overpotential differences ($\Delta\eta_{50}$) between these two electrolytes are 3, 31, and 5 for A-Co-NiSe₂, A-Co-NiO, and A-NiSe₂, respectively (Fig. 4b). The rather smaller $\Delta\eta_{50}$ values for A-Co-NiSe₂ and A-NiSe₂ are attributed to the repulsion of Cl⁻ by the self-derived SeO₄²⁻ SCL, which can be responsible for maintaining this high activity in the saline electrolyte. Furthermore, the lowest Tafel slope of A-Co-NiSe₂ (50 mV dec⁻¹) further supports its high electrocatalytic activity for the saline OER (Fig. 4c). Moreover, A-Co-NiSe₂ provides the largest ECSA among these catalysts that can offer easier diffusion of OH⁻ and H₂O and release of O₂ gas at the electrode/electrolyte interfaces, thus achieving the best ECSA-normalized OER activity (Fig. 4d and Fig. S23). We also examined if the SeO₄²⁻ on the catalyst surface affects the OER activity. The A-Co-NiSe₂ electrode was rinsed with fresh electrolyte to remove the SeO₄²⁻ adsorbed on the surface and then tested in a fresh electrolyte. The OER polarization curves before and after such operations show very limited activity differences (Fig. S24), indicating that the self-derived SeO₄²⁻ SCL hardly affects the activity of A-Co-NiSe₂.

Furthermore, we paired the A-Co-NiSe₂ on three-dimensional conductive copper foam as the anode with a Pt foil cathode for two-electrode electrolysis to evaluate the stability of the anode owing to the good activity and stability of Pt foil in electrolyte even with Cl⁻ [18]. As shown in Fig. 4e, the polarization curve of A-Co-NiSe₂ for the overall seawater splitting gives the cell voltage of 1.70 V at a current density of 500 mA cm⁻² in 1 M KOH + 0.5 NaCl, which is significantly lower than that of A-Co-NiO (~1.74 V at 500 mA cm⁻²). It is worth noting that the overpotential corresponding to this voltage (1.70 V) is lower than the equilibrium potential difference (~490 mV) between these two reactions of ClOR and OER under the alkaline condition, without triggering the oxidation of chloride to hypochlorite, which means a highly efficient seawater electrolysis on A-Co-NiSe₂. Especially, at 500 mA cm⁻², the Faradaic efficiency of O₂ on A-Co-NiSe₂ reaches about ~100% in 1 M KOH + 0.5 M NaCl (Fig. 4f and Fig. S25), while only ~58.6% for A-Co-NiO. The large difference in Faradaic efficiency was further confirmed by detecting oxidized chloride species (ClO⁻) in electrolytes through iodide titration [22]. As shown in Fig. S26, the electrolyte of A-Co-NiSe₂ remains a colorless transparent solution, suggesting that no reactive chloride species are generated during the OER

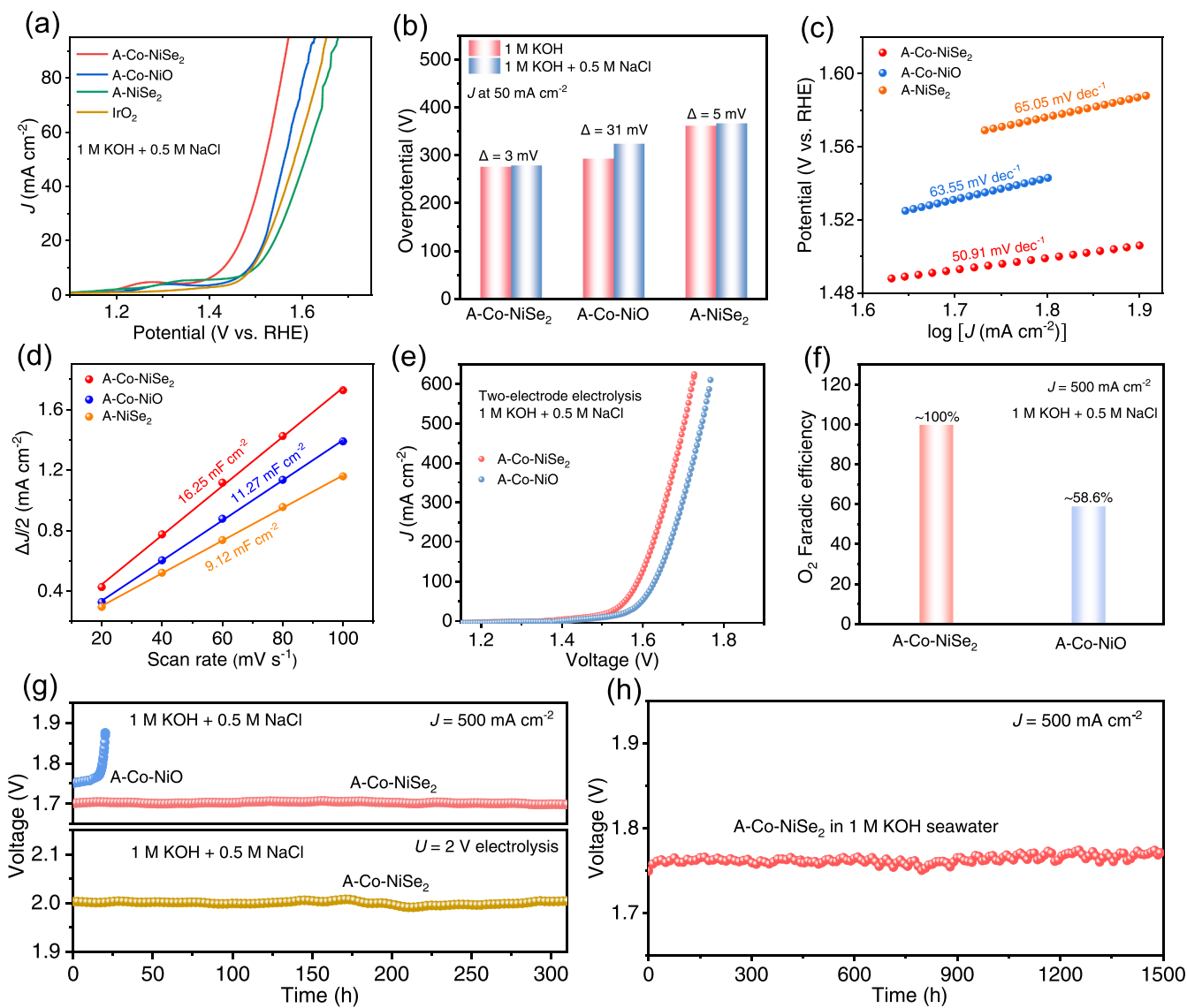


Fig. 4. (a) The OER polarization curves of A-Co-NiSe₂, A-Co-NiO, A-NiSe₂, and commercial IrO₂ in 1 M KOH + 0.5 M NaCl. (b) The corresponding overpotential differences between 1 M KOH and 1 M KOH + 0.5 M NaCl at 50 mA cm^{-2} . Tafel slopes (c) and ECSA values (d) of A-Co-NiSe₂, A-Co-NiO, and A-NiSe₂. (e) The two-electrode polarization curves in 1 M KOH + 0.5 M NaCl. Note that A-Co-NiSe₂ or A-Co-NiO loaded on copper foam is used as the anode and Pt foil as the cathode in the two-electrode system. (f) O_2 Faradaic efficiencies at 500 mA cm^{-2} in 1 M KOH + 0.5 M NaCl. (g) Long-term stability tests of seawater splitting at a constant current of 500 mA cm^{-2} for the A-Co-NiSe₂ and A-Co-NiO anodes in 1 M KOH + 0.5 M NaCl, as well as (h) the A-Co-NiO anode in 1 M KOH seawater.

process, while for A-Co-NiO, its electrolyte turns light yellow and deepens over time. Furthermore, to evaluate the long-term seawater splitting durability, chronopotentiometry measurements with a two-electrode system were performed in 1 M KOH + 0.5 M NaCl (Fig. 4g), in which the voltage of A-Co-NiSe₂ shows an unobvious change after 300 h tests at 500 mA cm^{-2} , and in contrast, A-Co-NiO quickly increases in potential within 20 h, suggesting rapid activity loss and catalyst deactivation. In order to meaningfully demonstrate the chlorine repulsion of the A-Co-NiSe₂ catalyst, we conducted seawater electrolysis with A-Co-NiSe₂ at a voltage of 2 V, much higher than the onset potential of the alkaline ClOR. Fig. 4g clearly shows that A-Co-NiSe₂ remains robust at a high voltage of 2 V in 1 M KOH + 0.5 M NaCl, accompanied by an unchanged solution color over 300 h of continuous electrolysis (Fig. S27). This remarkable durability highlights the role of chlorine corrosion resistance of the in-situ formed SeO₄²⁻ SCL during the anodic activation process. Furthermore, in 1 M KOH seawater (purified seawater), the voltage of A-Co-NiSe₂ does not fluctuate significantly within 1500 h (Fig. 4h, Fig. S28). Notably, this superior long-time

stability of A-Co-NiSe₂ at an industrial current density in 1 M KOH seawater is significantly better than those of most reported OER catalysts for seawater splitting (Table S1). More importantly, this unique SeO₄²⁻ SCL remains stable on the catalyst surface after long-term work (Fig. S29). In view of the fact that the in-situ formed SeO₄²⁻ shows resistance to chlorine corrosion, we are curious whether directly adding SeO₄²⁻ in the electrolyte can also improve the anti-corrosion performance of the catalyst. To this end, we took the A-Co-NiO catalyst as an example to test its corrosion resistance in alkaline simulated seawater containing selenate and as shown in Fig. S30, A-Co-NiO exhibits a certain degree of anti-corrosion performance, although it still declines at a rate of 0.25 mV h^{-1} . Compared with the anti-chlorine corrosion effect of our in-situ formed SeO₄²⁻ SCL, there is still a clear gap for artificial electrolyte engineering. This may be due to the competitive adsorption of added selenate ions and chloride ions. In contrast, the in-situ formed SeO₄²⁻ are more favorable for adsorption on the catalyst surface (Fig. S31), thereby more energetically repelling chloride ions from approaching the catalytic surface.

3.5. The anti-corrosion mechanism of the catalyst based on self-derived SeO_4^{2-} -SCL

To reveal the anti-corrosion behavior of the in-situ formed SeO_4^{2-} -SCL

on A-Co-NiSe₂, we studied the Zeta potential and potentiodynamic polarization curve test in 1 M KOH + 0.5 M NaCl. The Zeta potential results show that A-Co-NiSe₂ exhibits more negative Zeta potential (-40.5 mV) than A-Co-NiO (-22.6 mV) (Fig. 5a), indicating that it has

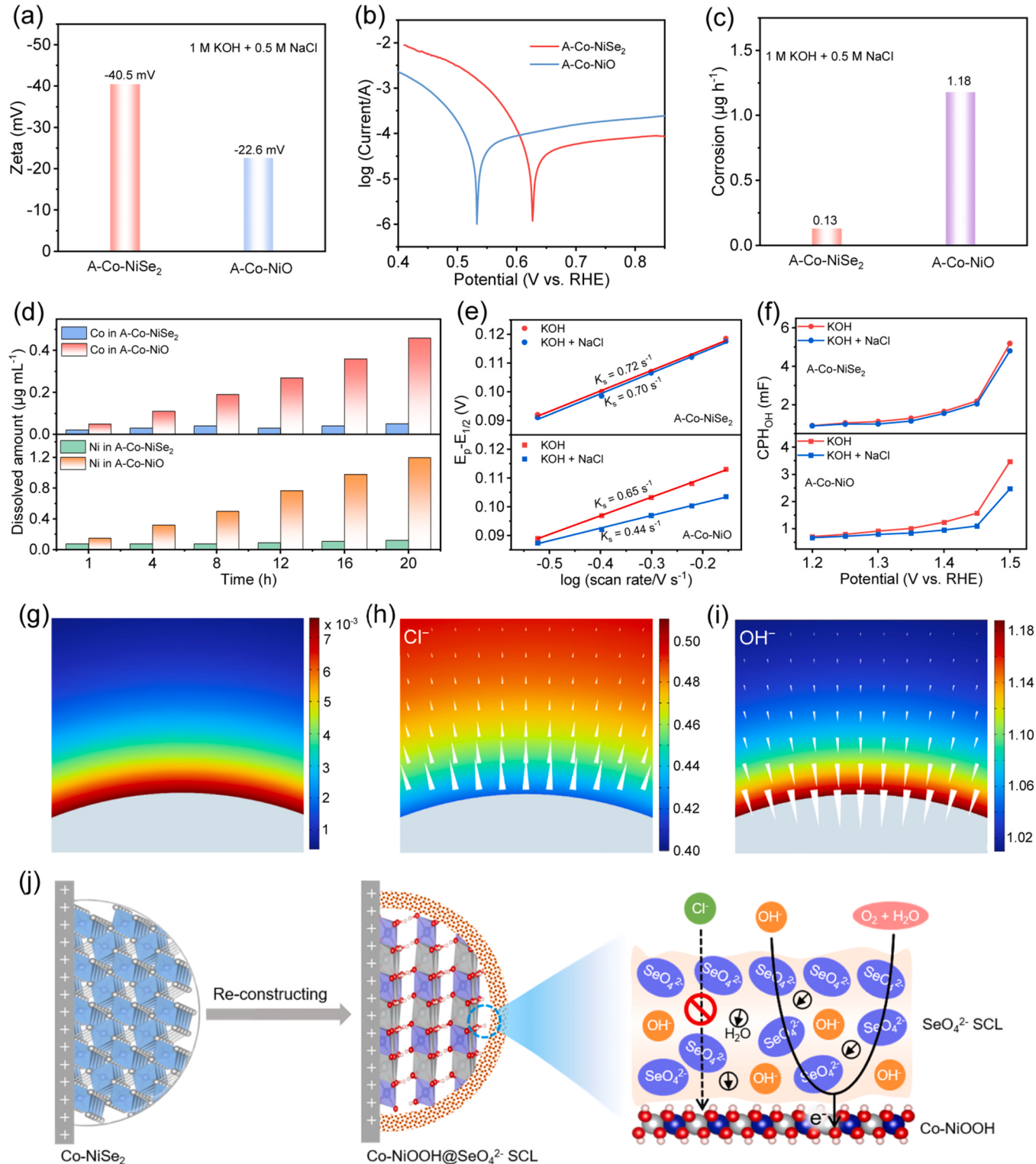


Fig. 5. (a) Zeta potentials, (b) potentiodynamic polarization plots, and (c) corrosion rates of the A-Co-NiSe₂ and A-Co-NiO electrodes in 1 M KOH + 0.5 M NaCl. (d) The leaching concentrations of Co and Ni ions of A-Co-NiSe₂ and A-Co-NiO anodes in the electrolyte during the test. (e) K_s values and (f) plots of CPE_{OH} versus the applied potential for A-Co-NiSe₂ and A-Co-NiO in 1 M KOH and 1 M KOH + 0.5 M NaCl. Finite element simulation analysis: (g) optimized model, surface Cl^- (h) and OH^- (i) density distribution on the electrode surface in simulated alkaline seawater. The arrows indicate the direction of concentration flux and the color represents the magnitude of ion concentration at the arrow's spatial position. (j) Illustration of the anti-corrosion mechanism of the SeO_4^{2-} -SCL on the electrode.

better chlorine-resistant ability owing to the electrostatic repulsion between the negatively charged A-Co-NiSe₂ and chloride ions. Furthermore, important information on parameters such as corrosion potential (E_{corr}), corrosion current (I_{corr}), and corrosion rate (V_{corr}) was carefully studied from potentiodynamic polarization curves. Generally, larger E_{corr} and lower I_{corr} together with a lower V_{corr} determine the corrosion resistive performance [48,49]. As shown in Fig. 5b, the E_{corr} of A-Co-NiSe₂ (0.627 V) moves to a more positive anodic potential region than that of A-Co-NiO (0.533 V), and meanwhile A-Co-NiSe₂ exhibits a smaller I_{corr} (8.20×10^{-5} A) compared with A-Co-NiO (1.14×10^{-4} A). The results demonstrate that A-Co-NiSe₂ has higher corrosion resistance than A-Co-NiO in the Cl⁻-containing condition, and this conclusion is further supported by the V_{corr} data (Fig. 5c), in which A-Co-NiSe₂ shows much lower V_{corr} value ($0.13 \mu\text{g h}^{-1}$) than A-Co-NiO ($1.18 \mu\text{g h}^{-1}$). In addition, the leaching amounts of the metal cations in the electrolyte during the test with or without the influence of SeO₄²⁻ SCL were determined by ICP-OES. As shown in Fig. 5d, almost negligible Co and Ni species in the electrolyte are detected for A-Co-NiSe₂ after 20 h, while as high as 0.46 and $1.2 \mu\text{g mL}^{-1}$ of Co and Ni exist in the electrolyte for A-Co-NiO, which are about 9 and 10 times higher than those of A-Co-NiSe₂ under the same conditions, respectively. The obvious discrepancy shows that A-Co-NiSe₂ has significant chloride-corrosion resistance in the presence of the in-situ formed SeO₄²⁻ SCL, which is thought to be an important reason for its excellent stability in alkaline seawater (Fig. 4h). To test the amount of Cl⁻ taken from the electrolyte, the solutions before and after the reaction were analyzed by ion chromatography (Fig. S32). Apparently, the amount of Cl⁻ absorption on A-Co-NiO increases substantially with increasing the electrolysis time, while a weak increase is observed for A-Co-NiSe₂ under the same conditions. These results reveal that the self-derived SeO₄²⁻ SCL can keep chloride ions away from the catalyst's surface due to electrostatic repulsion, thus preventing the coordination of Cl⁻ ions and accordingly inhibiting the dissolution of metal cations.

The dynamic anti-corrosion effect of the SeO₄²⁻ SCL was further reflected in the local environment of the electrode, especially the diffusion and adsorption of OH⁻ ions, which are important participants of OER. We first investigated the adsorption capacities of OH⁻ ions on the Ni sites of A-Co-NiSe₂ and A-Co-NiO in both 1 M KOH and 1 M KOH + 0.5 M NaCl by the Lavorin method. The steady redox currents all exhibit linear dependence on the square root of potential scan rate in CVs (5 to 700 mV s⁻¹, Figs. S33, S34), revealing that in alkaline solutions the redox kinetics of the metal sites are determined by the diffusion of OH⁻ ions from the electrolyte to electrode and coupling with the metal sites [50,51]. The redox constant (K_s) of A-Co-NiSe₂ is almost unchanged in these two electrolytes (0.72 s^{-1} vs 0.70 s^{-1}) (Fig. 5e), indicating that the SeO₄²⁻ SCL has little effect on the interaction of the catalyst with the OH⁻ ions, in line with the previous result where a rather smaller $\Delta\eta_{50}$ value for A-Co-NiSe₂ (Fig. 4b). In contrast, the K_s of A-Co-NiO in 1 M KOH + 0.5 M NaCl (0.44 s^{-1}) is obviously lower than that in 1 M KOH (0.65 s^{-1}), implying that the coupling of OH⁻ ions to Ni sites is restricted for A-Co-NiO in the Cl⁻-containing electrolyte, which leads to a decrease in the catalytic activity (Fig. 4b). This can be attributed to the fact that without the protection of the SeO₄²⁻ SCL, the accumulated Cl⁻ ions would replace the OH⁻ ions to competitively coordinate with the metal sites, thus resulting in the dissolution of the metal species. Besides, EIS is a useful electrochemical measurement to probe the properties of electrode/electrolyte interfaces and the adsorption kinetics of reactants on the electrode surface. *Operando* EIS was performed to get in-depth information on electrochemical reaction kinetics. Figs. S35a,b and Figs. S36a,b show the Nyquist plots of A-Co-NiSe₂ and A-Co-NiO from 1.20 to 1.50 V in 1 M KOH and 1 M KOH + 0.5 M NaCl. The resistances associated with the *OH intermediate (R_{OH}) in A-Co-NiSe₂ and A-Co-NiO at different applied potentials were quantified from the Nyquist plots based on the equivalent circuit (Fig. S37) [51]. It is obvious that in both 1 M KOH and 1 M KOH + 0.5 M NaCl, the R_{OH} values of these two catalysts decrease with increasing the potential, and

importantly the decrease is larger for A-Co-NiSe₂ within the applied potential range, implying its faster kinetics for adsorption of *OH. Notably, the R_{OH} difference between these two electrolytes is small for A-Co-NiSe₂ while large for A-Co-NiO (Figs. S35c, S36c), consistent with the K_s results. Meanwhile, the pseudocapacitance arising from *OH was defined as a constant phase element (CPE_{OH}), which was utilized to quantify the adsorption coverage of *OH [51]. Regardless of the electrolyte, the CPE_{OH} values of A-Co-NiSe₂ are higher than those of A-Co-NiO in the whole potential, indicating the higher coverage of *OH for A-Co-NiSe₂ (Fig. 5f). The fast *OH accumulation of A-Co-NiSe₂ should be in favor of the overall catalytic driving force. However, it is found that the CPE_{OH} value of A-Co-NiO decreases significantly across the whole potential range, while no obvious change is observed for A-Co-NiSe₂. The results demonstrate that the dynamic anti-corrosion behavior of the SeO₄²⁻ SCL repels chloride ions without significantly blocking the diffusion and adsorption of reactive species.

Moreover, we further employed finite-element-based simulations by COMSOL Multiphysics to reveal the effect of the SeO₄²⁻ SCL on the adsorption behaviors of Cl⁻ and OH⁻ ions on the anode. According to the morphology, size, and phase composition of the A-Co-NiSe₂ catalyst, we simply built a two-dimensional model (Fig. 5g), where the SeO₄²⁻ anions were pre-adsorbed on the model surface. The simulations suggest that the pre-adsorbed SeO₄²⁻ anion layer drives the Cl⁻ ions away from the model surface by electrostatic repulsion without affecting the diffusion and adsorption of OH⁻ ions to the surface (Fig. 5h,i). This may be due to that the SeO₄²⁻ anions have high electrochemical stability (difficult to be electrochemically oxidized) and large electrostatic potential to interact with H₂O molecules through hydrogen bonds, allowing the adsorbed SeO₄²⁻ to form a soft "semipermeable layer" with the surface H₂O to repel Cl⁻ without significantly hindering the diffusion of OH⁻ (Fig. 5j) [39]. This soft "semipermeable layer" is a three-dimensional skeleton that is mainly composed of adsorbed SeO₄²⁻ ions and surface H₂O molecules connected with intricate hydrogen bonding networks. Considering the abundant hydrogen bond interactions between SeO₄²⁻ ions and H₂O molecules, the transport of OH⁻ ions through the layer is favored. In contrast, since Cl⁻ ions are weak hydrogen bond acceptors, the coulombic repulsion between SeO₄²⁻ and Cl⁻ ions becomes dominant, and thus the diffusion of Cl⁻ ions within the layer is effectively inhibited.

3.6. Theoretical understanding of *in-situ* generated O_v contributing to OER activity

Previous experimental studies have shown that heteroatom doping with group VIII elements to form bimetallic oxyhydroxides could considerably modify or boost OER performance [43]. In our case, the *in-situ* XAS and EPR results together revealed abundant O_v existing in Co-NiOOH *in-situ* generated by Co-NiSe₂ reconstruction during the OER process. It is well addressed that the O_v can produce active sites and greatly affects the OER performance [52]. In fact, the *in-situ* generated Co-NiOOH with O_v for A-Co-NiSe₂ shows a high OER catalytic performance in both alkaline solution and simulated alkaline seawater. The role of Co-doping in promoting O_v formation can be understood in terms of the electronic structure. For Ni(III) in NiOOH, the electronic configuration is t_{2g}⁶e_g¹, and the d^z² orbital is occupied in a distorted crystal field due to the Jahn-Teller effect (Fig. 6a and Fig. S38) [53]. The doped Co (III) atoms are in a distorted octahedral crystal field dictated by the NiOOH matrix, induced by the asymmetric t_{2g}⁵e_g¹ filling of Co(III). Considering that the energy level of the unoccupied dx²-y² orbital of Co(III) is lower than that of Ni(III) by about 0.47 eV (Fig. S39), the excess electron prefers to occupy the lowest unoccupied orbital of Co (III), resulting in the conversion of Co(III) into Co(II). Thus, the doped Co (III) in the distorted crystal field is easier to be reduced into a lower valence state than Ni(III), thus leading to the formation of O_v around the Co atoms. Also, we further conducted first-principles calculations to explore whether the Co doping could promote the formation of O_v

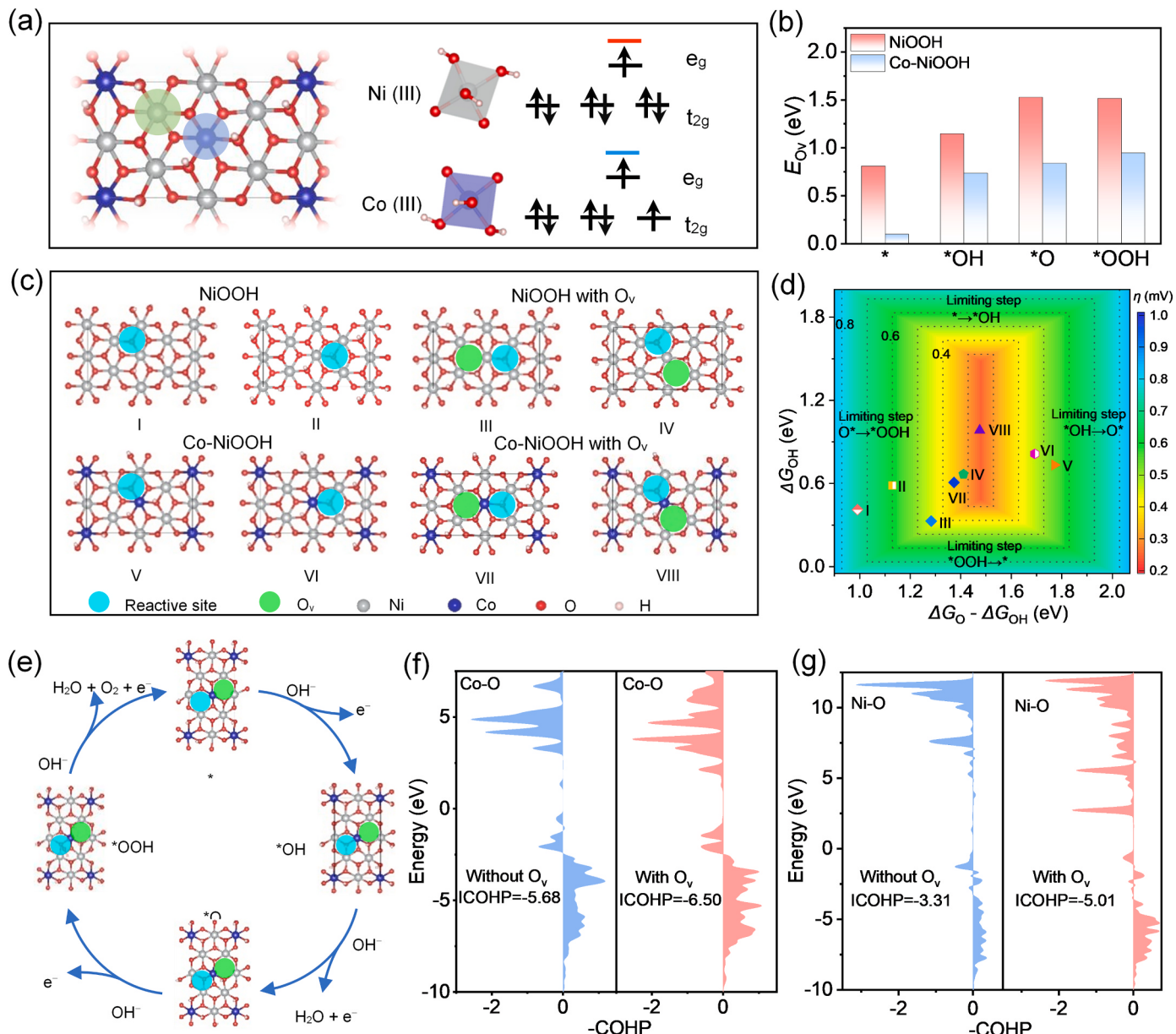


Fig. 6. (a) Atomic structure and the corresponding electronic configurations of the metal cations in Co-NiOOH. (b) Calculated E_{Ov} of NiOOH and Co-NiOOH during the OER process. (c) The possible reactive sites for the different systems. Structures I–IV represent NiOOH systems and structures V–VIII show Co-NiOOH systems. (d) Theoretical overpotential volcano plot for NiOOH with O* and *OH binding energies (ΔG_O and ΔG_{OH}) as descriptors, using the scaling relationship between *OH and *OOH ($\Delta G_{OOH} = \Delta G_{OH} + 2.96$ eV). All calculated overpotentials for the different sites of NiOOH, NiOOH with O_v, Co-NiOOH, and Co-NiOOH with O_v shown in (d) are contoured. Here, O*, *OH, and *OOH stand for the corresponding adsorption states. (e) Optimal reaction pathway for Co-NiOOH with O_v. COHP bonding analysis of the Co–O (f) and Ni–O (g) interactions in Co-NiOOH and Co-NiOOH with O_v. The Fermi levels are set to zero energy. The bonding interaction occurs at COHP larger than zero, whereas the antibonding interaction occurs at COHP smaller than zero.

during the OER process, which can proceed through a four-electron reaction in alkaline media. The calculated formation energies of O_v (E_{Ov}) for each step of OER are shown in Fig. 6b and Fig. S40. It is clear that the E_{Ov} values on Co-NiOOH decrease over the whole process compared to those on NiOOH, and the largest O_v formation energy is in step *OOH for Co-NiOOH (1.53 eV), but is in step *O for NiOOH (0.95 eV), and the energy difference within steps is within 0.7 eV. The results suggest that the Co doping can effectively enhance O_v formation by greatly reducing E_{Ov} . Considering the relatively small values of E_{Ov} and small energy differences between steps, the O_v should exist in the whole OER process under the applied potential. In general, we believe such O_v in Co-NiOOH is dynamically stable, and it will experience the cycle of generating, refilling, and regenerating during the OER reaction.

To explore the influence of O_v on the OER process, we investigated the free energies (ΔG) of the four-electron OER process for Co-free and Co-doped systems without and with O_v (Fig. 6c). The release of one O (I, IV, V, and VIII) or OH (II, III, VI, and VII) from NiOOH and Co-NiOOH creates three exposed metal ions, where further adsorption and reaction can occur. We calculated the overpotentials for all possible active sites, as shown in the volcano plot in Fig. 6d and Figs. S41–S48. In the case of NiOOH without O_v, the calculated overpotential for the OER is 0.60 V; the introduction of O_v substantially reduces the overpotential to 0.32 V. On the other hand, the formation of O_v in Co-NiOOH further decreases the overpotential to 0.25 V, approaching the theoretical peak of the OER volcano. Considering that O_v correlates with activity, NiOOH in A-NiSe₂ decreases the overpotential only a little, as observed in the

above experiment, while the Co-doped system further reduces the overpotential, which requires only 225 mV to 10 mA cm⁻². Thus, the formation of O_v is crucial for generating active sites, reducing the overpotential, and boosting OER activity. The optimal reaction pathway for Co-NiOOH with O_v is shown in Fig. 6e. Crystal orbital Hamilton population (COHP) analysis was then performed to investigate the bonding and antibonding states of the key intermediates (O^{*}) at the active metal atoms to gain insight into the high OER activity of as-formed Co-NiOOH with O_v (Fig. S49) [54–56]. As shown in Fig. 6f,g, the integrated COHP (ICOHP) values of Co–O and Ni–O in containing-O_v Co-NiOOH are – 6.50 and – 5.01, respectively, which are more negative than those of O_v-free Co-NiOOH, indicating less filling of the anti-bonding states of Co–O and Ni–O for containing-O_v Co-NiOOH [44]. According to the ICOHP theory [55], the more positive the ICOHP, the weaker the binding strength. Due to the weak strength between Co/Ni sites and O^{*} intermediates, the rate-determining step (RDS) for Co/Ni sites is the formation of O^{*} intermediates (*OH→O^{*}, see V or VI of Fig. 6e) in O_v-free Co-NiOOH. While for Co-NiOOH with O_v, owing to the strong binding strength, the RDS is the conversion of O^{*} to *OOH (O^{*}→*OOH, see VII or VIII of Fig. 6e). This explains why Co-NiOOH exhibits high OER activity with the assistance of O_v and highlights the importance of O_v for the OER process.

4. Conclusion

In summary, we developed Co-doped NiSe₂ (Co-NiSe₂) pre-catalyst for OER in alkaline seawater that evolves into the SeO₄²⁻ SCL-protected Co-NiOOH with high activity and corrosion resistance. In-situ experiments and theoretical investigations verified that the Co-doping for NiSe₂ not only facilitates its rapid self-reconstruction process, but also contributes to the generation of dynamically stable oxygen vacancy sites in Co-NiOOH. Notably, the formation of O_v is crucial for generating the active sites, reducing the overpotential, and boosting OER activity, and meanwhile this SeO₄²⁻ SCL at the electrode surface shows a dynamic anti-corrosion behavior, i.e. repelling Cl⁻ anions without blocking OH⁻ diffusion and thus preventing metal species dissolution. As a result, the A-Co-NiSe₂ catalyst can deliver an industrial current density (500 mA cm⁻²) at a cell voltage of 1.70 V with ~100% O₂ Faradaic efficiency, and durable seawater electrolysis for over 1500 h in real seawater electrolyte. This work provides a novel perspective toward understanding the protection mechanism of anions for OER electrocatalysts and would enlighten the development of simple yet efficient strategies to address the challenges in seawater electrolysis.

CRediT authorship contribution statement

Jie Zhu: Data curation, Formal analysis, Investigation, Methodology, Writing – original draft. **Baoguang Mao:** Conceptualization, Formal analysis, Writing – original draft. **Bo Wang:** Project administration, Supervision. **Minhua Cao:** Formal analysis, Supervision, Writing – review & editing.

Declaration of Competing Interest

The authors declare that they have no known competing financial interests or personal relationships that could have appeared to influence the work reported in this paper.

Data availability

Data will be made available on request.

Acknowledgements

This work was supported by the National Natural Science Foundation of China, China (No. 21872008) and the Natural Science Foundation of

Beijing, China (Grant No. 2212019). We would thanks to the Beamlines 1W1B at Beijing Synchrotron Radiation Facility (BSRF), China for the X-ray absorption fine structure (XAFS) and the Analysis & Testing Center of Beijing Institute of Technology for measurements. We would also like to thank Shiyanjia Lab (www.shiyanjia.com) for some characterizations.

Appendix A. Supporting information

Supplementary data associated with this article can be found in the online version at doi:[10.1016/j.apcatb.2023.123658](https://doi.org/10.1016/j.apcatb.2023.123658).

References

- [1] Z.W. Seh, J. Kibsgaard, C.F. Dickens, I. Chorkendorff, J.K. Norskov, T.F. Jaramillo, *Science* 355 (2017) aad4998.
- [2] H.P. Xie, Z.Y. Zhao, T. Liu, Y.F. Wu, C. Lan, W. Jiang, L.Y. Zhu, Y.P. Wang, D. S. Yang, Z.P. Shao, *Nature* 612 (2022) 673–678.
- [3] H. Ding, H.F. Liu, W.S. Chu, C.Z. Wu, Y. Xie, *Chem. Rev.* 121 (2021) 13174–13212.
- [4] L.K. Gao, X. Cui, C.D. Sewell, J. Li, Z.Q. Lin, *Chem. Soc. Rev.* 50 (2021) 8428–8469.
- [5] N. Wang, P. Ou, S.F. Hung, J.E. Huang, A. Ozden, J. Abed, I. Grigioni, C. Chen, R. K. Miao, Y. Yan, J. Zhang, Z. Wang, R. Dorakhan, A. Badreldin, A. Abdel-Wahab, D. Sinton, Y. Liu, H. Liang, E.H. Sargent, *Adv. Mater.* 35 (2023), e2210057.
- [6] L.B. Wu, L. Yu, F.H. Zhang, B. McElhenny, D. Luo, A. Karim, S. Chen, Z.F. Ren, *Adv. Funct. Mater.* 31 (2020), 2006484.
- [7] J.X. Guo, Y. Zheng, Z.P. Hu, C. Zheng, J. Mao, K. Du, M. Jaroniec, S.Z. Qiao, T. Ling, *Nat. Energy* 8 (2023) 264–272.
- [8] Y. Kuang, M.J. Kenney, Y. Meng, W.H. Hung, Y. Liuf, J.E. Huanga, R. Prasannag, P. Li, Y. Li, L. Wang, M.C. Lin, M.D. McGehee, X. Sun, H. Daia, *PNAS* 116 (2019) 6624–6629.
- [9] L.Z. Zhuang, J.K. Li, K.Y. Wang, Z.H. Li, M.H. Zhu, *Adv. Funct. Mater.* 32 (2022), 2201127.
- [10] W.H. Hung, B.Y. Xue, T.M. Lin, S.Y. Lu, I.Y. Tsao, *Mater. Today Energy* 19 (2021), 100575.
- [11] X.H. Wang, Y. Ling, B. Wu, B.L. Li, X.L. Li, J.L. Lei, N.B. Li, H.Q. Luo, *Nano Energy* 87 (2021), 106160.
- [12] S. Wu, Y.C. Zhu, G.S. Yang, H. Zhou, R.Q. Li, S. Chen, H.G. Li, L.M. Li, O. Fontaine, J. Deng, *Chem. Eng. J.* 446 (2022), 136833.
- [13] Tu Haq, Y. Haik, *Appl. Catal. B Environ.* 334 (2023), 122853.
- [14] J. Liu, S. Duan, H. Shi, T. Wang, X. Yang, Y. Huang, G. Wu, Q. Li, *Angew. Chem. Int. Ed.* 134 (2022), e202210753.
- [15] X. Kang, F. Yang, Z. Zhang, H. Liu, S. Ge, S. Hu, S. Li, Y. Luo, Q. Yu, Z. Liu, Q. Wang, W. Ren, C. Sun, H.M. Cheng, B. Liu, *Nat. Commun.* 14 (2023) 3607.
- [16] L. Tan, J.T. Yu, C. Wang, H.F. Wang, X. Liu, H.T. Gao, L.T. Xin, D.Z. Liu, W.G. Hou, T.R. Zhan, *Adv. Funct. Mater.* 32 (2022) 2200951.
- [17] R. Liu, R. Tang, J. Feng, T. Meng, *Chem. Eng. J.* 470 (2023), 144261.
- [18] T. Ma, W. Xu, B. Li, X. Chen, J. Zhao, S. Wan, K. Jiang, S. Zhang, Z. Wang, Z. Tian, Z. Lu, L. Chen, *Angew. Chem. Int. Ed.* 60 (2021) 22740–22744.
- [19] D.L. Wu, D. Chen, J.W. Zhu, S.C. Mu, *Small* 17 (2021), e2102777.
- [20] Tu Haq, Y. Haik, *ACS Sustain. Chem. Eng.* 10 (2022) 6622–6632.
- [21] H. Zhang, H. Han, X. Yang, H. Ma, Z. Song, X. Ji, *Catal. Sci. Technol.* DOI:[10.1039/D3CY01085F](https://doi.org/10.1039/D3CY01085F).
- [22] H.H. You, D.S. Wu, D.H. Si, M.N. Cao, F.F. Sun, H. Zhang, H.M. Wang, T.F. Liu, R. Cao, *J. Am. Chem. Soc.* 144 (2022) 9254–9263.
- [23] J. Liang, Z. Li, X. He, Y. Luo, D. Zheng, Y. Wang, T. Li, B. Ying, S. Sun, Z. Cai, Q. Liu, B. Tang, X. Sun, *Mater. Today* 69 (2023) 193–235.
- [24] J.K. Li, F. Xu, K. Wang, J. He, Y.X. Wang, L.F. Lei, M.H. Zhu, L.Z. Zhuang, Z. Xu, *Chem. Eng. Sci.* 267 (2023), 118366.
- [25] X. Xu, H. Liao, L. Huang, S. Chen, R. Wang, S. Wu, Y. Wu, Z. Sun, H. Huang, *Appl. Catal. B Environ.* 341 (2024), 123312.
- [26] H. Zhang, X. He, K. Dong, Y. Yao, S. Sun, M. Zhang, M. Yue, C. Yang, D. Zheng, Q. Liu, Y. Luo, B. Ying, S. Alfaifi, X. Ji, B. Tang, X. Sun, *Mater. Today Phys.* 38 (2023), 101249.
- [27] M. Yue, X. He, S. Sun, Y. Sun, M.S. Hamdy, M. Benaissa, A.A.M. Salih, J. Liu, X. Sun, *Nano Res.* DOI:[10.1007/s12274-023-6002-6](https://doi.org/10.1007/s12274-023-6002-6).
- [28] L. Yu, Q. Zhu, S.W. Song, B. McElhenny, D.Z. Wang, C.Z. Wu, Z. Qin, J.M. Bao, Y. Yu, S. Chen, Z.F. Ren, *Nat. Commun.* 10 (2019) 5106.
- [29] Tu Haq, M. Pasha, Y. Tong, S.A. Mansour, Y. Haik, *Appl. Catal. B Environ.* 301 (2022), 120836.
- [30] J.Z. Liu, L. Guo, *Adv. Mater.* 4 (2021) 2850–2873.
- [31] H. Zhang, S. Geng, M. Ouyang, H. Yadegari, F. Xie, D.J. Riley, *Adv. Sci.* 9 (2022), e2200146.
- [32] Y. Wang, W.L. Yu, Bo. Wen Zhou, W.P. Xiao, J.S. Wang, X.P. Wang, G.G. Xu, B. Li, Z.J. Li, Z.X. Wu, L. Wang, J. Mater. Chem. A 11 (2023) 1886.
- [33] T.Z. Wu, Y.M. Sun, X. Ren, J.R. Wang, J.R. Song, Y.D. Pan, Y.B. Mu, J.S. Zhang, Q. Z. Cheng, G.Y. Xian, S.B. Xi, C.M. Shen, H.J. Gao, A.C. Fisher, M.P. Sherburne, Y. H. Du, Joel W. Ager, J. Gracia, H.T. Yang, L. Zeng, Z.C.J. Xu, *Adv. Mater.* 35 (2023), e2207041.
- [34] H. Lei, L. Ma, Q.X. Wan, S.Z. Tan, B. Yang, Z.L. Wang, W.J. Mai, H.J. Fan, *Adv. Energy Mater.* 12 (2022), 2202522.
- [35] M. Kim, B. Lee, H. Ju, S.W. Lee, J. Kim, *Adv. Mater.* 31 (2019), 1901977.
- [36] X. Xu, S. Zhang, Q. Zhang, S. Chen, Y. Wu, Z. Sun, *ACS Sustain. Chem. Eng.* 11 (2023) 15338–15349.

[37] F. Sun, J.S. Qin, Z.Y. Wang, M.Z. Yu, X.H. Wu, X.M. Sun, J.S. Qiu, *Nat. Commun.* 12 (2021) 4182.

[38] Tu Haq, Y. Haik, *Small Sci.* 2 (2022), 2200030.

[39] M. Yu, J.H. Li, F.M. Liu, J.D. Liu, W.C. Xu, H.L. Hu, X.J. Chen, W.C. Wang, F. Y. Cheng, *J. Energy Chem.* 72 (2022) 361–369.

[40] B.S. Zhang, S. Liu, S.J. Zhang, Y. Cao, H.L. Wang, C.Y. Han, J. Sun, *Small* 18 (2022), e2203852.

[41] Y. Hu, Y. Zheng, J. Jin, Y. Wang, Y. Peng, J. Yin, W. Shen, Y. Hou, L. Zhu, L. An, M. Lu, P. Xi, C.H. Yan, *Nat. Commun.* 14 (2023) 1949.

[42] N. Zhang, Y. Hu, L. An, Q. Li, J. Yin, J. Li, R. Yang, M. Lu, S. Zhang, P. Xi, C.H. Yan, *Angew. Chem. Int. Ed.* 61 (2022), e202207217.

[43] T.Z. Wu, S.G. Sun, J.J. Song, S.B. Xi, Y.H. Du, B. Chen, W.A. Sasangka, H.B. Liao, C. L. Gan, G.G. Scherer, L. Zeng, H.J. Wang, H. Li, A. Grimaud, Z.J. Xu, *Nat. Catal.* 2 (2019) 763–772.

[44] Z.F. Huang, J.J. Song, Y.H. Du, S.B. Xi, S. Dou, J.M.V. Nsanzimana, C. Wang, Z. Chuan, J. Xu, X. Wang, *Nat. Energy* 4 (2019) 329–338.

[45] Y.M. Shi, W. Du, W. Zhou, C.H. Wang, S.S. Lu, S.Y. Lu, B. Zhang, *Angew. Chem. Int. Ed.* (50) (2020) 22470–22474.

[46] J. Zhu, M. Sun, S.J. Liu, X.H. Liu, K. Hu, L. Wang, *J. Mater. Chem. A* 7 (2019) 26975–26983.

[47] M.K. Trivedi, K.K. Sethi, P. Panda, S. Jana, *Marmara Pharm. J.* 21 (2017) 311, 311.

[48] J. Li, Y. Liu, H. Chen, Z. Zhang, X. Zou, *Adv. Funct. Mater.* 31 (2021), 2101820.

[49] S.M. Sun, Y.M. Sun, Y. Zhou, J.J. Shen, D. Mandler, R. Neumann, *Chem. Mater.* 31 (2019) 8106–8111.

[50] J. Wang, L. Gan, W. Zhang, Y. Peng, H. Yu, Q. Yan, X. Xia, X. Wang, *Sci. Adv.* 4 (2018), eaap7970.

[51] P.L. Zhai, C. Wang, Y.Y. Zhao, Y.X. Zhang, J.F. Gao, L.C. Sun, J.G. Hou, *Nat. Commun.* 14 (2023) 1873.

[52] Z. Xiao, Y.C. Huang, C.L. Dong, C. Xie, Z. Liu, S. Du, W. Chen, D. Yan, L. Tao, Z. Shu, G. Zhang, H. Duan, Y. Wang, Y. Zou, R. Chen, S. Wang, *J. Am. Chem. Soc.* 142 (2020) 12087–12095.

[53] J.X. Kang, X.Y. Qiu, Q. Hu, J. Zhong, X. Gao, R. Huang, C.Z. Wan, L.M. Liu, X. F. Duan, L. Guo, *Nat. Catal.* 4 (2021) 1050–1058.

[54] J. Ma, Q. Zhi, L. Gong, Y. Shen, D. Sun, Y. Guo, L. Zhang, Z. Xia, *Nanoscale* 12 (2020) 19375–19382.

[55] L. Qiu, G. Zheng, Y. He, L. Lei, X. Zhang, *Chem. Eng. J.* 409 (2021), 128155.

[56] T. Meng, P. Sun, F. Yang, J. Zhu, B. Mao, L. Zheng, M. Cao, *PNAS* 119 (2022), e2214089119.